Available online at www.sciencedirect.com
SCIENCE DIRECT®
Journal of Solid State Chemistry 177 (2004) 2833–2840
JOURNAL OF SOLID STATE CHEMISTRY
http://elsevier.com/locate/jssc

# The dielectric function of *Ln*SF rare-earth fluorosulfides (*Ln*= La, Ce): experiment and theory

Fabrice Goubin,[a] Xavier Rocquefelte,[a] Damien Pauwels,[b] Alain Tressaud,[b] Alain Demourgues,[b,1] Stephane Jobic,[a,*] and Yvan Montardi[c]

[a] *Laboratoire de Chimie des Solides, Institut des Matériaux Jean Rouxel, UMR 6502, Université de Nantes—CNRS, 2 rue de la Houssinière, BP 32229, 44322 Nantes Cedex 03, France*

[b] *Institut de la Matière Condensée de Bordeaux, CNRS, avenue du Dr. A. Schweitzer, 33608 Pessac Cedex, France*

[c] *RHODIA, Centre de Recherches d'Aubervilliers, 52 rue de la Haie-Coq, 93308 Aubervilliers Cedex, France*

Received 6 March 2004; received in revised form 4 May 2004; accepted 9 May 2004

**Abstract**

The absorption properties of LaSF and CeSF in the UV-Visible range have been investigated on the basis of first principles density functional theory (DFT) calculations and from electron energy-loss spectroscopy (EELS) measurements. The extinction coefficient $k$, as well as the refractive index $n$, determined experimentally from the loss function $\mathrm{Im}(-1/\varepsilon)$, were compared with the corresponding factors extracted from the calculated dielectric tensor $\varepsilon_2$. The $k$ and $n$ values for the two compounds were expected to be very close to each other, owing to the chemical similarity of La and Ce. However, it was found that the nature of the electronic transitions in LaSF and CeSF strongly influences the $k$ and $n$ values with the result that the refractive index $n$ and the extinction coefficient $k$ are substantially larger for LaSF than for CeSF.
© 2004 Elsevier Inc. All rights reserved.

*Keywords:* Lanthanide thiofluoride; Optical properties; Band structures; Dielectric constants; EELS

## 1. Introduction

Owing to their prospective industrial interest as inorganic pigments and/or UV blockers, sunlight absorbing inorganic phases have received much attention during the last decade. The strong incentive to develop new colored inorganic materials originates from the necessity to get rid of current heavy-elements-based industrial pigments that are hazardous to health and environment [1]. For instance, to compete with widely used pigments such as $CdS_{1-x}Se_x$, $PbCrO_4$,…, only a few yellow and red risk-free materials are available at present on the market. As far as inorganic UV absorbers are concerned, the discovery of new ones is motivated by the need to have better absorbing materials to prevent the deterioration of various materials such as wood and plastic and the harm done to the biological tissues exposed to UV radiation [2,3]. To reduce the UV light damages done to an organic matter, UV rays can be blocked either by using opaque pigments or by employing transparent UV absorbers that selectively absorb the harmful radiation. Based on esthetic criteria, highly colored materials have only a limited use whereas colorless UV absorbers find wider applications [4]. It should be pointed out that the development of new pigments and particle-based sunscreens requires the knowledge of the optical properties of the inorganic materials, that is, their opacity (i.e., the light scattering power) and their color strength (i.e., the light absorbing capacity) as pure phases and in dispersion medium. The intrinsic properties of pigments and UV blockers are fully contained in their dielectric function $\varepsilon$, which describes the linear response of an insulator electronic system to an applied electrical field. Actually, the propagation of an electromagnetic wave through a material can be described by the complex refractive index $N(\lambda) = n(\lambda) + ik(\lambda)$, which is mathematically related to $\varepsilon(\lambda)$. $n$ and $k$, which are the refractive index and the extinction coefficient, respectively, depend on the wavelength $\lambda$ of the incident radiation. In vacuum, $N$

*Corresponding author. Fax: +33-2-40-37-39-95.
*E-mail address:* jobic@cnrs-imn.fr (S. Jobic).
[1] Also for correspondence.

0022-4596/$ - see front matter © 2004 Elsevier Inc. All rights reserved.
doi:10.1016/j.jssc.2004.05.006

is real and equal to 1. It is also real for materials transparent in the visible range, but it is complex for absorbing materials, the imaginary part being related to the absorption coefficient $\alpha$, according to $\alpha = 4\pi k/\lambda$. $\varepsilon$ can be decomposed as a real part $\varepsilon_1$, related to the polarisability of the electronic system, and as an imaginary part $\varepsilon_2$, originating from electronic transitions. The relation between the real and imaginary parts of the refractive index and the dielectric function can be written as $\varepsilon_1 = n^2 + k^2$ and $\varepsilon_2 = 2nk$.

The major difference between insulating pigments and UV absorbers do not lie only in the position of the absorption threshold but also in the value of the refractive index. Hence, light scattering in the visible range has to be minimized in UV absorbers (low $n$ index), while the opposite is requested for coloring pigments (high $n$ index). Based on these facts, $TiO_2$ is to be regarded as a white pigment even if transparent grade for UV blocker applications can be made by manufacturing particles with an extremely small particle size ($\varnothing \approx 15$ nm [5]) to limit the rather strong light scattering.

Recently, alkali metal and/or alkaline earth cerium substituted $\gamma$-$Ce_2S_3$ phases have been proposed as pigments with colors ranging from red burgundy to orange [6–9]. They are currently at the stage of industrial production [10]. When Ce is substituted by another rare-earth metal, a color change is indeed observed. Hence the substitution of Sm for Ce leads to the yellow $\gamma$-$Sm_2S_3$ compound. Likewise, the substitution of other anions for sulfur will lead to interesting color modifications. In fact, the modification of the chemical bond covalency will affect the optical band gap, the absorption coefficient as well as the refractive index $n$. Hence, the synthesis and the characterization of new (oxy)fluorosulfides have been investigated recently. It turns out that the introduction of fluorine in the coordination sphere of the rare-earths lead to the stabilization of numerous, colored, new compounds [11].

In the present article, we describe the experimental and theoretical determination of the dielectric function in *Ln*SF (*Ln* = La, Ce) in order to gain insight into the origin of the color in these materials and the optical constants $n(\lambda)$ and $k(\lambda)$.

## 2. Experimental section

*Ln*SF compounds (*Ln* = La, Ce) were synthesized as described elsewhere [12]. Electron energy loss spectroscopy (EELS) characterization of the powders were carried out on a transmission electron microscope (TEM) Philips CM 30, $LaB_6$ gun, coupled with a GATAN 666 spectrometer controlled through ELP3 software to derive the optical constants of the phases. The TEM was operated at 100 kV, with an unsaturated beam, to optimize the spectral resolution. An FWHM of 0.8 eV was routinely achieved in these conditions. The image-coupling mode was used, where the diffraction pattern is sent in the aperture of the spectrometer. The following parameters were chosen: entrance aperture diameter of 2 mm, energy dispersion of 0.1 eV and acquisition time below 500 ms. Spectra acquisition was made in nanoprobe mode on a 10–20 nm diameter area. Electron diffraction pattern was qualitatively used to select thin area and avoid crystals whose orientation corresponded to a simple crystallographic axis parallel to the electron beam. The convergence angle (3.5 mrad) was high enough not to make the analysis orientation dependent. Eight spectra were acquired, aligned and summed up together. Acquisition and comparison of the spectra translated on the photodiode array made it possible to insure that low intensity features on the spectra in the energy range 2–5 eV were not due to "ghost" or persistent effect after exposing the photodiode array with zero loss high intensity peak, a problem GATAN 666 spectrometer is sensitive to.

Classically, the treatment of the spectra followed four steps: (i) extraction of data and deconvolution of multiple diffusion effects; (ii) correction for acquisition parameters (convergence and collection angles); (iii) normalization using "$n_0$" refractive index extrapolated to low energy (2.45 for LaSF and 2.10 for CeSF); (iv) Kramers–Krönig analysis using numerical integration methods. The mathematical relationships behind steps 2 and 3 have been described in detailed by Egerton [13] and Montardi et al. [14]. We emphasize here the first step of the procedure, which is the most important for insuring reliability of the results. Most of the procedures employed rely on the modeling of the zero loss peak using Gaussian and Lorenztian components and in removing this model from the raw spectrum. Our experience shows that this method strongly underestimates the high-energy part of the elastic peak, leading to an overestimation of the intensity of the low-energy part of $\mathrm{Im}(-1/\varepsilon)$. This effect, detectable below 10 eV, influences greatly the results below 5 eV. The procedure generates also artifacts in the 0–3 eV region. This problem can be overcome as follows: firstly, we extract the relevant information from the raw spectrum using a model for the high-energy side of the zero loss using a $A \cdot E^{-r}$ power law imbedded in the ELP software for the background subtraction. The energy window (1 eV) used for fitting was placed below the optical gap for the product. Various data can be used for this purpose: the known gap, the powder color, diffuse reflection measurements, etc. The accurate position is tested for minimum artifact and the useful signal is then retrieved using the "background subtraction" function in the ELP program. Secondly, we compute a model of the zero loss peak using the computed thickness function in ELP: a composite spectrum is then constructed by adding the Zero Loss peak model with the extracted

data. The behavior of this spectrum in the ELP's Fourier ratio deconvolution procedure gave good results. The $I'(E)$ function obtained is simply related to $\mathrm{Im}(-1/\varepsilon(E))$ by a scale factor $K$.

As the thickness of the measured area is not known with a good accuracy, the determination of this scale factor $K$ was made using the Kramers–Kronig relation at $E = 0\,\mathrm{eV}$:

$$1 - \mathrm{Re}\left[\frac{1}{\varepsilon(0)}\right] = 1 - \frac{1}{n_0^2} = \frac{2}{\pi}\int_0^\infty \mathrm{Im}\left[\frac{-1}{\varepsilon(E)}\right]\frac{\mathrm{d}E}{E}. \quad (1)$$

In this expression $\mathrm{Im}(-1/\varepsilon(E))$ may be replaced by $I'(E)$ in order to define the summation rule

$$K = \frac{(2/\pi)\int_0^\infty (I'(E)/E)\,\mathrm{d}E}{1 - \mathrm{Re}(1/\varepsilon(0))}. \quad (2)$$

For insulating materials, absorption and therefore $\varepsilon_2$ is negligible at $E = 0\,\mathrm{eV}$. The real part of the dielectric function can be simplified as follows:

$$\mathrm{Re}\left(\frac{1}{\varepsilon(0)}\right) \approx \frac{1}{\varepsilon_1(0)} \approx \frac{1}{n_0^2}, \quad (3)$$

where "$n_0$" is the refraction index in the infrared region. Practically, as we cannot measure and take into account the phonon absorption phenomena, "$n_0$" is the extrapolated value of $n$ when $E$ is nearing 0 eV, and has therefore no physical meaning. Obviously, with the new materials reported here, one should note that the "$n_0$" value remains unknown and has to be fixed near the experimental value obtained by optical analysis (refractometry and ellipsometry) on single-crystals whose crystal structures and chemical compositions are close to those of new compounds. For this reason, the dielectric constant was calculated for a series of hypothetical $n_0$. The result presented here corresponds to the best agreement between the measure and the estimation from band structure calculations.

Finally, since the loss function is a causal response, the real part of the dielectric function can be calculated from the imaginary part with the Kramers–Krönig relation:

$$\mathrm{Re}\left(\frac{1}{\varepsilon(E)}\right) = 1 - \frac{2}{\pi}P\int_0^\infty \mathrm{Im}\left(\frac{-1}{\varepsilon(E)}\right)\frac{E'}{E'^2 - E^2}\,\mathrm{d}E', \quad (4)$$

where $P$ is the principal part of the Cauchy integral.

Finally, the $\varepsilon_1$ and $\varepsilon_2$ parts of the complex dielectric function can be deduced from $\mathrm{Im}(-1/\varepsilon(E))$ and $\mathrm{Re}(1/\varepsilon(E))$ by the relations

$$\varepsilon_1(E) = \frac{\mathrm{Re}(1/\varepsilon(E))}{\mathrm{Re}(1/\varepsilon(E))^2 + \mathrm{Im}(-1/\varepsilon(E))^2} \quad (5)$$

and

$$\varepsilon_2(E) = \frac{-\mathrm{Im}(-1/\varepsilon(E))}{\mathrm{Re}(1/\varepsilon(E))^2 + \mathrm{Im}(-1/\varepsilon(E))^2}. \quad (6)$$

## 3. Computational details

### 3.1. Band structure calculations

Our calculations are based on the density functional theory (DFT). The Perdew–Burke–Ernzerhof generalized gradient approximation (GGA) was used for the exchange and correlation correction [15]. The density of states and the complex part of the dielectric function are deduced from a self-consistent calculation, using the Full-potential Linearized Augmented Plane Wave (FP-LAPW) method, as embodied in the WIEN2k code [16]. The maximum $l$ value in the expansion of the basis set inside an atomic sphere was 12 for the computation of muffin-tin matrix and 4 for the non-muffin-tin matrix element. The convergence of basis set is controlled by a cutoff parameter $R_{\mathrm{mt}} \times K_{\max} = 8$ where $R_{\mathrm{mt}}$ is the smallest atomic sphere radius in the unit cell and $K_{\max}$ is the magnitude of the largest $k$ vector. The self-consistency were carried out on a 20 $k$-points mesh in the irreducible Brillouin zone, with the following radii $R_{\mathrm{mt}}(\mathrm{La, Ce}) = 2.91$ a.u., $R_{\mathrm{mt}}(\mathrm{S}) = 2.3$ a.u., $R_{\mathrm{mt}}(\mathrm{F}) = 1.93$ a.u. and $G_{\max} = 14\,\mathrm{Bohr}^{-1}$ for the *Ln*SF calculations.

### 3.2. Optical properties calculations

The dielectric function of an anisotropic material is a complex symmetric second order tensor. The imaginary part of the dielectric tensor is directly related to the electronic band structure of a solid, so it can be computed from the knowledge of the single-particle orbitals and energies approximated by the solutions of the Kohn–Sham equations. Assuming the one-electron, rigid band approximations, neglecting electron polarization effects (Koopmans' approximation) and in the limit of linear optics and of the visible-ultraviolet region [17,18], the imaginary part of a matrix element of the dielectric tensor is given by

$$\varepsilon_2(\omega) = \frac{4\pi^2 e^2}{m^2\omega^2}\sum_{i,f}\int_{BZ}\frac{2\mathrm{d}k}{(2\pi)^3} |\langle \varphi_{f\,k}|\boldsymbol{e}\cdot\boldsymbol{p}|\varphi_{ik}\rangle|^2\delta(E_f(\omega) - E_i(\omega) - \hbar\omega) \quad (7)$$

for a vertical transition from a filled initial state $|\varphi_{ik}\rangle$ of energy $E_i(k)$ to an empty final state $|\varphi_{f\,k}\rangle$ of energy $E_f(k)$, with wave vector $k$. $\omega$ is the frequency, $e$ the electron charge, $m$ the free electron mass, $\mathbf{p}$ the momentum operator and $\mathbf{e}$ the polarization. $\varepsilon_2$ was systematically calculated up to $\hbar\omega$ equal to 40 eV. $\varepsilon_2$ can be viewed as detailing the real transitions between occupied and unoccupied electronic states. For this reason, the $f \to f$ transitions and the valence band $\to f$ electronic transitions were not taken into account in its calculation for CeSF. Since the dielectric function describes a causal response, the real and imaginary

parts are linked by a Kramers–Kronig transformation. This is used to obtain the real part $\varepsilon_1(\omega)$, a lorentzian broadening of 0.05 eV being considered. In order to get the isotropic dielectric function, the components of the matrix trace were averaged (i.e. $\varepsilon_{iso} = 1/3(\varepsilon_{xx} + \varepsilon_{yy} + \varepsilon_{zz})$). The complex refractive index was thus calculated with the formulas given above. For the dielectric tensor calculation, the *BZ* integration was made with 63 independent *k*-points. Finer *k*-point grids did not modify the dielectric tensors values. No scissors operator was introduced in the present study, that is, no shift of the bands situated above valence band was applied as usually carried out [19,20]. This choice was validated a posteriori by the good agreement between experiment and calculation (vide infra).

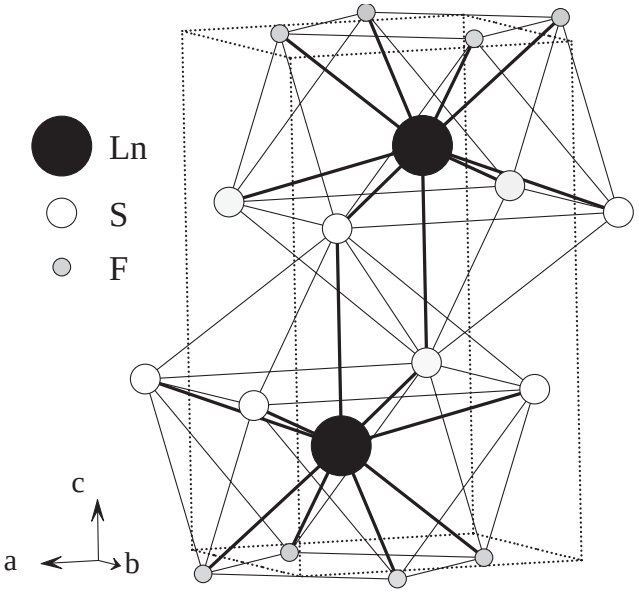


Fig. 1. *Ln*SF structure, with $LnS_5F_4$ polyhedron.

## 4. Results and discussion

The *Ln*SF phases (*Ln* = La, Ce) crystallize with the BiOCl (PbFCl) structure type [12], a very common tridimensional structure for substances containing two different-sized anions. The structure can be described as an intergrowth of $[Ln_2F_2]^{4+}$ fluorite-type blocks and $[S_2]^{4-}$ double sulfur sheets (Fig. 1). The layers alternate along the stacking axis with the regular sequence $-[F^- - Ln^{3+} - S^{2-} - S^{2-} - Ln^{3+}]-$ and nine-coordinate rare-earth atoms are surrounded by four fluorine atoms and five sulfur atoms (i.e. four plus one sulfur atoms belonging to two distinct sulfur sheets). The *Ln* environment can be viewed as a distorted monocapped $[LnF_4S_5]$ square antiprism with nearly identical *Ln*–S distances. S–S distances are all long enough to rule out any anion-anion interaction and the occurrence of $[S_2]$ dimers. From Kubelka–Munk transformed diffuse reflectance measurements, pale yellow LaSF and red CeSF exhibit a steep absorption threshold at 2.80 and 2.08 eV, respectively [12].

### 4.1. Band structures of LaSF and CeSF

The total density of states (DOS) for LaSF is displayed in Fig. 2a in the $[-6, +8]$ eV energy range. The calculated band dispersion along some high-symmetry directions of the Brillouin zone is depicted

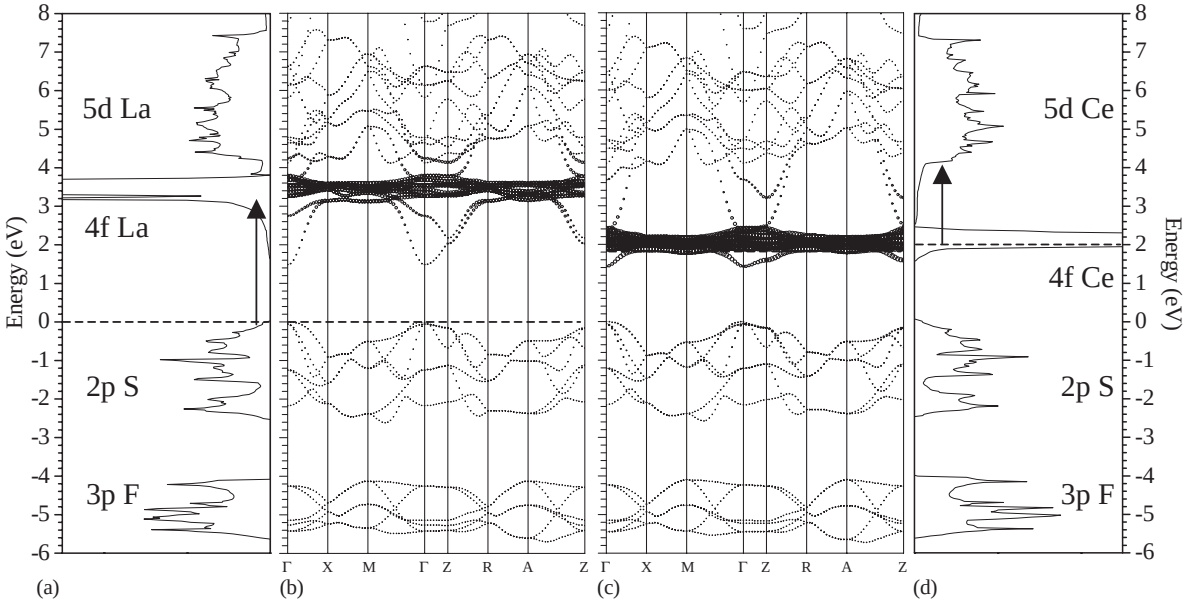


Fig. 2. Total density of state (DOS) and band dispersion along high symmetry axis for LaSF, (a) and (b), and CeSF (c) and (d).

in Fig. 2b, where the contribution of the *Ln*–4*f* orbitals is emphasized by means of a "fat band" visualization, that is, a fattening of the energy dispersion lines proportional to the orbital characters. The zero energy is arbitrarily taken at the Fermi level (dashed line).

In the [−6,0] eV range lies the valence band (vb), which can be clearly divided in two blocks separated by 1.5 eV. The lower energy part is mainly built upon F 2*p* orbitals while the highest one, almost exclusively, consists of S 3*p* orbitals. This sequencing is related to the much stronger electronegativity of fluorine compared to that of sulfur ($\chi^S = 2.58$ and $\chi^F = 3.98$ according to Pauling). Above the Fermi level, the conduction band (cb) lies from 1.5 eV and consists of two distinct sets of bands. The La 5*d* orbitals give rise to a broad band with dispersed energy levels. In contrast, the rare-earth 4*f* orbitals, located just above the bottom of the cb, may be regarded as completely localized. Because the lowest states of the conduction band are exclusively La 5*d* orbitals in character and because these levels are very dispersed, the DOS at the bottom of the cb is very low and almost insignificant compared to the La 5*d* contribution above 4 eV (Figs. 2a and b). In contrast, the DOS associated with the *f* contribution has a sharp peak due to the very strong localization of the *f* levels. In view of the band structure features, the yellowish color of LaSF and the measured 2.80 eV optical gap may be attributed to a charge transfer excitation from S to La, that is, the promotion of a S 3*p* electron towards the first unoccupied La 5*d* orbitals. This scheme is quite appealing since the highest occupied orbital and the lowest unoccupied orbital are located at the $\Gamma$ point implying a direct transition ($\Delta k = 0$). The discrepancy between the observed optical gap and the calculated one could then only originate in the well-known limitation of DFT to predict energy gap (gap usually calculated at 60% or 70% of the true value). However, because of the very low density of states at the bottom of the cb, it is reasonable to consider that the optical absorption would be mostly due to an S 3*p* → La 4*f* transition rather than a S 3*p* → La 5*d* one. From calculations, the latter would take place at about 1.5 eV, whereas the former would occur at around 2.8 eV in remarkable and unexpected good agreement with the experimental optical gap [12]. Nevertheless, let us mention at this stage that experiments carried out on rare-earth trihalides using inverse photoemission spectroscopy [21] positioned La 4*f* orbitals significantly higher in energy compared to the present model. Unfortunately, no such data are reported so far on LaSF in the literature for comparison between experiment and theory.

The band structure and total DOS of CeSF are given in Figs. 2c and d with the last occupied level highlighted by a dotted line. To better discuss the evolution of the band positioning going from LaSF to CeSF, the DOS was rescaled in energy on the S 1*s* core level (the F 1*s* core level taken as reference gave the same results) while the origin of the energies was maintained at the top of the vb in LaSF.

The DOS and the band dispersion of CeSF exhibit similar features to those of LaSF, the main difference lying in the stabilization in energy of the Ce 4*f* block, now interspaced between the S 3*p* anionic band and the *Ln* 5*d* cationic band. The width, the shape and the location in energy of the F 2*p*, S 3*p* and *Ln* 5*d* blocks are practically not affected by the La/Ce substitution. Note that the long, low-energy tail of the *Ln* 5*d* block is now better seen owing to the stabilization of the *f* block. Of course, due to the electron counting, the Fermi level for CeSF is shifted higher in energy compared to LaSF: it is now positioned within the 1/14th occupied 4*f* block. Because of the localized character of the *f* orbitals, the unpaired electron cannot lead to a metallic behavior, its effective mass tending toward infinity. For this reason, CeSF has to be regarded as an insulator and the red color originates unambiguously from the promotion of a Ce 4*f* electron towards the cb, i.e. a $4f \rightarrow 5d$ intra-atomic transition. The occurrence of a $3p(S) \rightarrow 4f^1$ electronic transition or an intersite $4f^1 + 4f^1 \rightarrow 4f^0 + 4f^2$ mechanism can be ruled out since the energy needed to add an extra electron on a $Ce^{III}$ site is estimated at about 6 eV due to a strong on-site repulsion (Hubbard energy). The $4f-5d$ calculated energy gap is estimated at about 0.5 eV from DFT calculations, that is far from the expected value of 2 eV. Nevertheless, as mentioned for LaSF, because of the low density of states at the bottom of the cb, it would appear more realistic to consider an optical transition from the Ce 4*f* block towards the significant DOS area of the 5*d*(Ce) block, which corresponds to the energy of the *d*-levels located above 4 eV in Fig. 2d. In that case, the absorption threshold associated to the $4f \rightarrow 5d$ transition is found again to be in good agreement with the measurements (2.08 eV).

### 4.2. Refractive index (*n*) and extinction coefficient (*k*) of LaSF and CeSF

Figs. 3a and b display the variation of Im($\varepsilon$), *k* and *n* as a function of *E* (the energy of the incident radiation) for LaSF and CeSF, respectively. For both compounds, a satisfactory agreement is found between the experimental EELS and the calculated isotropic imaginary part of the complex dielectric functions in the 0–15 eV range. Hence, without using a scissors operator, the present DFT calculations reproduce the experimental data. Such an agreement was clearly unexpected because of the inherent problem of underestimating the band gap and inadequate descriptions of *f* orbitals by the DFT.

For LaSF, the calculated $\varepsilon_2(E)$ curve evidences three well-distinct peaks centered at about 4, 6.5 and 11.5 eV.

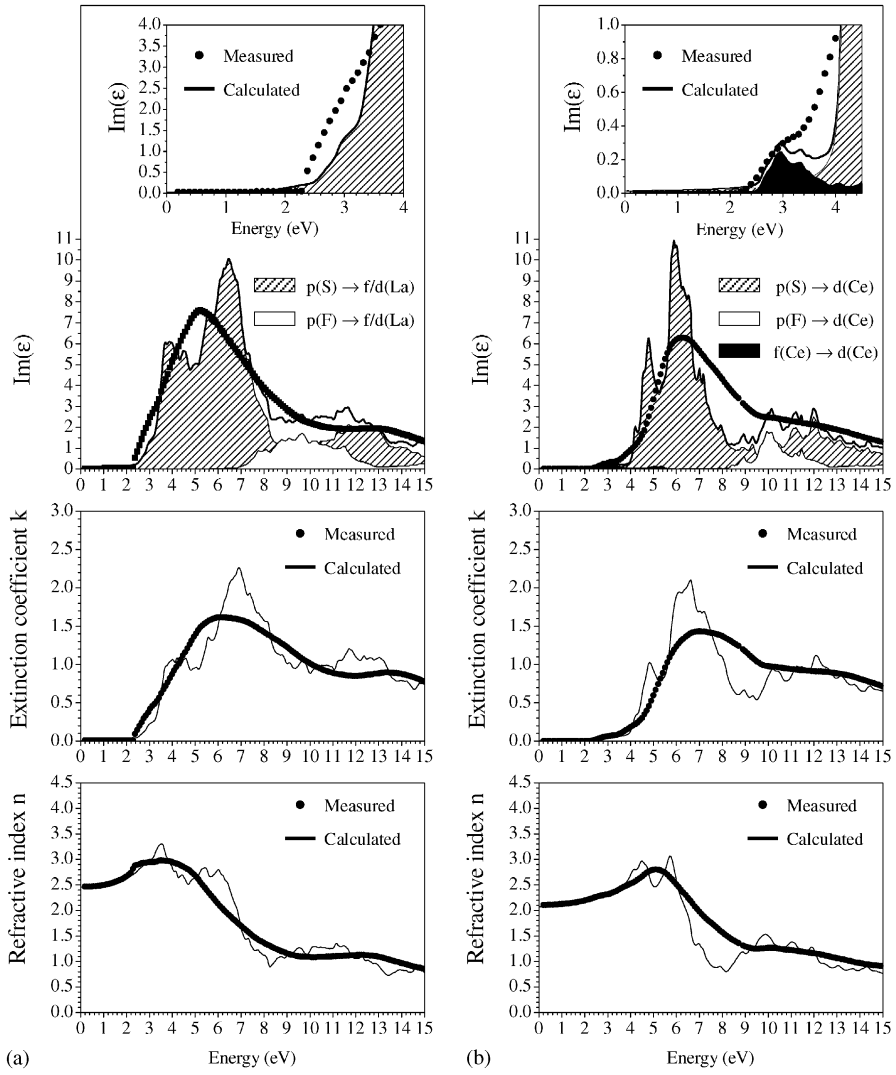


Fig. 3. Measured and calculated isotropic imaginary part of the dielectric function $\mathrm{Im}(\varepsilon)$, extinction coefficient $k$ and refractive index $n$ in the 0–15 eV range, for LaSF (a) and CeSF (b). The different transitions contributions are also given for $\mathrm{Im}(\varepsilon)$, namely S $3p \rightarrow$ La $4f/5d$, F $2p \rightarrow$ La $4f/5d$ transitions for LaSF and S $3p \rightarrow$ Ce $5d$, F $2p \rightarrow$ Ce $5d$ and Ce $4f \rightarrow 5d$ transitions for CeSF.

The two first, which collapse into one in the experimental curve, originate from the S $3p \rightarrow$ La $4f/5d$ transitions ($4f$ orbitals contribution is almost limited to the first peak at 4 eV) while the last one is associated with the overlap of a F $2p \rightarrow$ La $4f/5d$ transition and a S $3p \rightarrow$ La $5d$ one (see Figs. 2a and b). However, as highlighted in the inset, the occurrence of a long tail (from 1.5 to 2.4 eV) followed by a pre-peak centered at 2.8 eV is clearly evidenced. They can be assigned to the electronic transitions from the vb towards the lowest energy dispersed La $5d$ levels of the cb and the first unoccupied La $4f/5d$ hybridized levels, respectively. This latter transition explains the shoulder observed experimentally around 3 eV on the $\mathrm{Im}(\varepsilon)$ curve.

The overall shape of the $\mathrm{Im}(\varepsilon)$ response of CeSF is comparable to that of LaSF. The main difference lies in the happening of a pre-peak centered at about 3 eV (in black in Fig. 3b) originating from a Ce $4f^1 \rightarrow$ Ce $5d^0$ transition with no significant contribution of the lowest dispersed Ce $5d$ levels of the cb (vide supra). Although the $f \rightarrow d$ transition is parity and spin allowed, its contribution to $\varepsilon_2$ is nearly insignificant in intensity compared to the S($p$)$\rightarrow$Ce($d$) transition located higher in energy. Such a phenomenon has already been observed in cerium borates [22]. Thus, even if Ce $4f$ states are usually not properly described, it turns out that in the present case the band structure well explains experiment.

The general feature of $k(E)$ of LaSF and CeSF seems to be very similar to that of the imaginary part of $\varepsilon$. At first sight, the La derivative appears more absorbing (higher overall $k$ values) than the Ce one. This can be related to the disappearance of the $4f$ levels as "acceptors levels" in CeSF compared to LaSF. At the

end, the refractive index at about 2.1 eV (i.e., at the yellow sodium doublet emission) is estimated at ~2.6 and ~2.2 for LaSF and CeSF, respectively, while the zero frequency limit of the refractive index $n_0$ is calculated at ~2.5 and ~2.10, respectively. Notice that a rough calculation based on the Gladstone–Dale formula [23] yields a refractive index of about 2.5 and 2.4 in the near infra red region for the lanthanum and cerium derivatives (with $n(Ln_2S_3) \sim 2.7$ [24] and $n(LnF_3) \sim 1.6$ according to manufacturers ($Ln$ = La, Ce)) to compared to $n_0$. Due to the expected similarity in the La–ligand and Ce–Ligand bonding, the difference in the refractive indices originates probably from the nature of the electronic transition that strongly varies from LaSF to CeSF compounds. As pointed out above, the real and imaginary part of $\varepsilon$ are linked by the Kramers–Kronig relationship. Written for $\hbar\omega = 0$ eV, this gives:

$$\varepsilon_1(0) = 1 + \frac{2}{\pi}\int_0^{+\infty} \frac{\varepsilon_2(\omega')}{\omega'}\,d\omega'. \quad (8)$$

Thus, since $\varepsilon_1(0) = n_0^2 \sim n^2$, the higher the $\varepsilon_2(\omega)/\omega$ ratio, the greater $n_0$ and $n$.

To summarize, the substitution of $Ce^{3+}$ ($4f^1$) for $La^{3+}$ ($4f^0$) induces a strong decrease in the optical gap, due to a strong stabilization of the 4*f*-block in energy, and a concomitant lowering of the refractive index, which is related to the absence of an allowed S $3p \rightarrow Ln$ $4f$ transition for Ce. Then, the change in the refractive index in the *Ln*SF series ($Ln$ = La, Ce) is not correlated to a modification of the ionocovalency of the *Ln*-Ligand bonding ($\chi^{La} = 1.10$, $\chi^{Ce} = 1.12$ according to Pauling), but rather to the nature (and the intensity) of the electronic transitions at work, i.e., only a charge transfer in LaSF versus an intrasite Ce $4f \rightarrow$ Ce $5d$ transition and a less intense charge transfer in CeSF.

## 5. Conclusion

The present work was focused on the determination and the understanding of the optical properties of LaSF and CeSF. Due to the inherent difficulty of estimating the refractive index of a powder sample, no experimental data were available so far. The use of a dual approach that coupled EELS experiments with DFT calculations allowed us to estimate the refractive indices and the extinction coefficients of LaSF and CeSF. Nevertheless, these *absolute* values would have to be confirmed by refractometry and ellipsometry measurements on large single crystals while the positioning in energy of the La $4f$ and Ce $4f$ orbitals have to be experimentally determined using Bremsstrahlung isochromat and photoemission spectroscopies.

The DFT simulations, without using any scissor operator, were found to be in very good agreement with the EELS experimental data. The refractive index at 589 nm decreases from LaSF (2.6) to CeSF (2.2). Such an evolution cannot be explained by the empirical approach that states that the refractive index increases as a function of the "mass" density ($\rho_{LaSF=} 5.54\ g\,cm^{-3}$ and $\rho_{CeSF=} 5.73\ g\,cm^{-3}$) [23,25]. The decrease in $n$ from the low-density (LaSF) to the high-density (CeSF) compound is explained on the basis of the $\varepsilon_2$ spectrum decomposition in its different contributions. While LaSF has a high index value attributable to a charge transfer transition from S $3p$ to La $4f$, CeSF has a lower index value related to the absence of a S $3p \rightarrow Ln$ $4f$ transition and the occurrence of an intrasite Ce $4f \rightarrow$ Ce $5d$ transition inducing a significant decrease in the capability of CeSF to absorb the overall visible and UV light as compared to LaSF (i.e. $\int_0^{+\infty} (\varepsilon_2(\omega')/\omega')\,d\omega'$ is larger for LaSF than for CeSF).

Due to its color and its refractive index, CeSF appears appropriate for a pigment application. Owing to its pale yellow hue and its higher refractive index, LaSF could be only considered as a potential UV blocker, and only if extra fine particles can be prepared to minimize the scattering coefficient of the materials in the visible range.

## Acknowledgments

F.G., X.R. and S.J. thank Pr. M.-H. Whangbo for valuable discussions.

## References

[1] European Economic Community Guideline no. 91/338/EWG, 1991.
[2] M.A. Pathak, in: N.J. Lowe, N.A. Shaath, M.A. Pathak (Eds.), Sunscreens: Development, Evaluation, and Regulatory Aspects, Vol. 15, Marcel Dekker, Inc., Phoenix, 1997.
[3] J.F. Rabek, Photodegradation of Polymers: Physical Characteristics and Applications, Springer, Berlin, 1996.
[4] D. Fairhurst, M.A. Mitchnick, in: N.J. Lowe, N.A. Shaath, M.A. Pathak (Eds.), Sunscreens: Development, Evaluation, and Regulatory Aspects, Vol. 15, Marcel Dekker, Inc., Phoenix, 1997.
[5] http://www.sachtleben.de/h/e/anw/0340e.html
[6] T. Chopin, H. Guichon, O. Tourret, EP545746, December 4, 1991.
[7] P. Maestro, EP0203838, April 30, 1985.
[8] P. Macaudière, EP680930, May 6, 1995.
[9] P. Maestro, D. Huguenin, J. Alloys Compds. 225 (1995) 520.
[10] http://www.rhodia-rare-earths.com
[11] D. Pauwels, A. Demourgues, H. Laronze, et al., Solid State Sci. 4 (2002) 1471.
[12] A. Demourgues, A. Tressaud, H. Laronze, et al., J. Alloys Compds. 323–324 (2001) 223.
[13] R.F. Egerton, Electron Energy Loss Spectroscopy in the Electron Microscope, Plenum Press, New-York, 1986.
[14] Y. Montardi, C. Witz, L. Normand, et al., J. Phys. IV 9 (1999) 217.
[15] J.P. Perdew, S. Burke, M. Erzenrhof, Phys. Rev. Lett. 77 (1996) 3865.

[16] P. Blaha, K. Schwartz, G.K.H. Madsen, et al., in: WIEN2K an Augmented Plane Wave + Local Orbitals Program for Calculating Crystal Properties, Techn. Universität Wien, Austria, 2001.
[17] W.D. Lynch, in: E.D. Palik (Ed.), Handbook of Opticals Constants of Solids, Academic Press, New York, 1985.
[18] F. Bassani, G. Pastori Parravicini, R.A. Ballinger, Electronic States and Optical Transitions in Solids, Pergamon Press, Oxford, 1975.
[19] P. Puschnig, C. Ambrosch-Draxl, Phys. Rev. B 60 (1999) 7891.
[20] R. Del Sole, R. Girlanda, Phys. Rev. B 48 (1993) 11789.
[21] K.-H. Park, S.J. Oh, Phys. Rev. B 48 (1993) 14833.
[22] F. Goubin, Y. Montardi, P. Deniard, X. Rocquefelte, R. Brec, S. Jobic, J. Solid State Chem. 177 (2004) 89.
[23] R. Tilley, Colour and the Optical Properties of Materials, Wiley, New York, 2000.
[24] C. Witz, Thesis of Paris VI, Université Pierre et Marie Curie, 1995.
[25] X. Rocquefelte, F. Goubin, H-J. Koo, M-H. Whangbo, S. Jobic, Inorg. Chem. 43 (2004) 2246.